Adaptive noise estimation from highly textured hyperspectral images

Peng Fu,[1,2] Changyang Li,[2] Yong Xia,[3] Zexuan Ji,[1] Quansen Sun,[1,*]
Weidong Cai,[2] and David Dagan Feng[2]

[1]School of Computer Science and Engineering, Nanjing University of Science and Technology, Nanjing 210094, China

[2]School of Information Technologies, The University of Sydney, Sydney, NSW 2006, Australia

[3]School of Computer Science, Northwestern Polytechnical University, Xi'an 710072, China

*Corresponding author: sunquansen@njust.edu.cn

Accurate approximation of noise in hyperspectral (HS) images plays an important role in better visualization and image processing. Conventional algorithms often hypothesize the noise type to be either purely additive or of a mixed noise type for the signal-dependent (SD) noise component and the signal-independent (SI) noise component in HS images. This can result in application-driven algorithm design and limited use in different noise types. Moreover, as the highly textured HS images have abundant edges and textures, existing algorithms may fail to produce accurate noise estimation. To address these challenges, we propose a noise estimation algorithm that can adaptively estimate both purely additive noise and mixed noise in HS images with various complexities. First, homogeneous areas are automatically detected using a new region-growing-based approach, in which the similarity of two pixels is calculated by a robust spectral metric. Then, the mixed noise variance of each homogeneous region is estimated based on multiple linear regression technology. Finally, intensities of the SD and SI noise are obtained with a modified scatter plot approach. We quantitatively evaluated our algorithm on the synthetic HS data. Compared with the benchmarking and state-of-the-art algorithms, the proposed algorithm is more accurate and robust when facing images with different complexities. Experimental results with real Airborne Visible/Infrared Imaging Spectrometer (AVIRIS) images further demonstrated the superiority of our algorithm.   © 2014 Optical Society of America

OCIS codes: (100.0100) Image processing; (100.4145) Motion, hyperspectral image processing; (280.0280) Remote sensing and sensors; (110.2960) Image analysis.
http://dx.doi.org/10.1364/AO.53.007059

1. Introduction

In hyperspectral (HS) imaging systems, HS spectrometers adopt narrow band intervals, resulting in weak energy acquired within each band. Consequently, the quality of HS images could be easily degraded by noise influence [1–3]. In practice, noise type and level are unknown in advance. Therefore, correct approximation of noise type and accurate estimation of noise level for HS images can benefit subsequent image processing in, for example, HS image restoration [4], classification [5] and target detection [6].

Generally, the noise in HS images can be divided into two categories: random noise and pattern noise. In this paper, we focus mainly on random noise, which is still challenging to remove completely, while the pattern noise can be removed by an accurate radiometric calibration or by applying destriping algorithms [7]. Traditionally, the random noise in HS images is often assumed to be purely additive and, thereby, independent of original signal data. When the additive noise is approximated by normal

distribution with zero mean, the noise variance can be treated as the measure of additive noise level [7–15]. However, recent studies show that, with improvement of sensitivity in electronic components, the random noise can be modeled as a mixture of signal-dependent (SD) noise and signal-independent (SI) noise for a part of HS images [16–19]. SD noise is commonly referred to as photon noise, which occurs when a sensor collects photons. Actually, the number of photons collected by one cell of a CCD detector fluctuates according to the Poisson distribution, whose expected value is proportional to the radiance of the surface element imaged by the cell of the CCD [16,20–23].

Under the assumption of purely additive noise, noise estimation of HS images is an active research topic. Fujimoto *et al.* [8] proposed an algorithm to approximate the variance of noise by computing the variance of pixel values in a homogeneous area. The disadvantage is that the homogeneous area is selected manually, which is time consuming and makes it difficult to judge the homogeneity of an area. Remote-sensing images with high spatial resolution often contain a large number of small homogeneous areas. Based on this observation, Gao [10] developed an automatic algorithm by dividing an image into many small blocks and calculating local means and local standard deviations of these blocks, then estimating the noise by using a histogram statistical algorithm. To better approximate the noise variance of small blocks, Corner *et al.* [7] utilized data-masking technology by assuming that image textures are generally smoother than noise. However, it is still a weakness that all of the aforementioned algorithms focus only on extracted information from each individual band in HS data and fail to take spectral information into account. To better utilize the information from high spectral resolution of HS images, a spectral and spatial decorrelation (SSDC) algorithm [11] based on the multiple linear regression (MLR) model was proposed to estimate noise. The residuals of the MLR model are considered to be noise, while the signal of a pixel at a particular band can be described as a linear combination of the neighboring pixels in the same band and the same spatial pixels in immediately adjacent bands. This algorithm is reliable on uniform images but is always difficult to use to deal with highly textured images for the lack of accurate detection of homogeneous areas. Gao *et al.* [12] proposed an object-seeking algorithm to segment the image into different classes to detect the homogeneous regions. However, the object-seeking algorithm was reported [14] to be defective and the similarity metric in this algorithm often has difficulty discriminating two classes, which makes it unreliable when estimating noise from HS images.

Based on the mixed noise assumption, there are generally two main steps to estimating intensities of the SD and SI noise [16–22]. The splitting of noise and the original signal from a HS image is usually the first step in these algorithms. Then, maximum likelihood estimation (MLE) and scatter plot are two main approaches for the calculation of the SD and SI noise in the second step. Acito *et al.* [17] proposed a fully automatic algorithm to extract noise and signal from an original image with spectral information without any free parameter. However, the accuracy of split noise and signal may be reduced without the spatial information. To solve this issue, the algorithm in [19] introduced a mixture of spectrally correlated fractal Brownian motion samples and random noise by jointly processing the HS data with a locally 3D scanning window. In [19], noise was proved to be of a mixture type in Airborne Visible/ Infrared Imaging Spectrometer (AVIRIS) images, and the SD and SI noise were estimated from a single scanning window. Because of the high computational complexity, the algorithm is not widely applied. In summary, MLE-based algorithms suffer from two disadvantages: sensitivity in initial value selection and high computational complexity for the optimal solution.

In [21], a classical algorithm was proposed to estimate both purely additive and multiplicative noise based on the scatter plot approach. An image is divided into blocks or windows with a rather small size, a scatter plot of local mean on local noise variance is estimated, and finally, curve fitting is carried out with the points in the scatter plot. The scatter-plot-based algorithm can be easily extended to deal with mixed noise estimation, where the slope and intercept of the fitted line correspond to the intensities of SD and SI noise, respectively. Because of textures and edges in the image, there are always abundant "abnormal" points generated from textured image blocks, which can seriously affect the veracity of curve fitting. In [18], Alparone *et al.* attempted to eliminate the abnormal points by dividing the whole image into nonoverlapping blocks and detecting homogeneous ones first. The weakness of this algorithm is that it requires a manually selected homogeneous area for the calculation of the homogeneity judgment threshold, which mainly determines the accuracy of noise estimation. An advanced algorithm was proposed in [22], in which homogeneous blocks are selected automatically with a global homogeneity threshold, which is calculated on the most densely populated bins of the binned scatter plot from the image. To find the most densely populated bins, a global threshold parameter is introduced and set empirically for any given image. This algorithm produces high accuracy on mixed noise estimation, particularly when structures in the HS image are simple.

One of the most challenging tasks is to accurately estimate noise from highly textured HS images with abundant edges and textures, as the homogeneous areas in these images are difficult to detect precisely. Another challenge is that noise type is assumed to be either purely additive or mixed in conventional assumptions, which will limit the scope of their applications. In this paper, we propose a novel

algorithm that can adaptively estimate noise from HS images with various complexities and different noise types. To better deal with the highly textured HS images, an automatic homogeneous-area-detection algorithm is proposed based on the region-growing approach. A robust spectral metric is utilized to determine the similarity of two pixels in a spatial band, making the homogeneous-area-detection algorithm more stable with random noise existing in the image. Furthermore, our algorithm can accurately estimate both purely additive noise and mixed noise without identifying their types beforehand.

For the sake of completeness in presentation, Section 2 introduces a generalized two-parameter noise model for HS images. Section 3 describes the proposed noise estimation algorithm in detail. Section 4 shows a comparison between the proposed algorithm and four considered algorithms both on synthetic images and real HS data. Moreover, an application of our algorithm is also presented. Section 5 draws the conclusions of this study.

2. Noise Model for Hyperspectral Images

A generalized noise model was proposed to deal with different types of noise in [20]. The observed HS image can be formulated by

$$g(t,s,p) = f(t,s,p) + n(f(t,s,p)), \tag{1}$$

where (t,s) is the pixel location in spatial space and p is the band number. $g(t,s,p)$ represents the observed noisy HS image, $f(t,s,p)$ is the original noise-free image signal, and $n(f(t,s,p))$ denotes the random noise. The original image signal is modeled as a nonstationary process that is strongly correlated between-band due to the high spectral resolution. In contrast, the noise in the HS image is generally assumed to be uncorrelated in the spectral and spatial domains [17,18]. The random noise is composed of two mutually independent parts and can be written as

$$n(f(t,s,p)) = n_{\text{si}}(t,s,p) + n_{\text{sd}}(f(t,s,p)), \tag{2}$$

in which $n_{\text{si}}(t,s,p)$ is a SI noise component and $n_{\text{sd}}(f(t,s,p))$ is a SD noise component. The SI noise component is generated mainly from electronics, while the SD noise results mainly from the photon noise. Note that the SD noise will be significant in physical scenarios such as nighttime imaging, astronomy, and ultraspectral systems.

In terms of distributions, the SI noise and SD noise are characterized as follows:

$$n_{\text{si}}(t,s,p) \sim N(0, \sigma_{\text{si}}^2),$$
$$\chi(f(t,s,p) + n_{\text{sd}}(f(t,s,p))) \sim \pi(\chi f(t,s,p)), \tag{3}$$

where σ_{si}^2 is the variance of the SI noise and χ is a real scalar parameter. N and π denote the Gaussian distribution and the Possion distribution. From the properties of Possion distribution, we can get the mean and variance as follows:

$$E\{\chi(f(t,s,p) + n_{\text{sd}}(f(t,s,p)))\} = \chi f(t,s,p),$$
$$V\{\chi(f(t,s,p) + n_{\text{sd}}(f(t,s,p)))\} = \chi f(t,s,p), \tag{4}$$

where $E\{\cdot\}$ and $V\{\cdot\}$ are defined as the expected value and variance of a random variable. Since $E\{\chi(f + n_{\text{sd}}(f))\} = \chi f + \chi E\{n_{\text{sd}}(f)\}$ and $\chi^2 V\{n_{\text{sd}}(f)\} = \chi f$ (pixel locations are omitted here for simplified notations), we can obtain that

$$E\{n_{\text{sd}}(f(t,s,p))\} = 0, V\{n_{\text{sd}}(f(t,s,p))\} = f(t,s,p)/\chi. \tag{5}$$

Accordingly, the noise variance model can be written as

$$\sigma_n^2 = \sigma_{\text{si}}^2 + \sigma_{\text{sd}}^2 \cdot f(t,s,p), \tag{6}$$

where $\sigma_{\text{sd}}^2 = 1/\chi$. σ_n^2 and $\sigma_{\text{sd}}^2 \cdot f(t,s,p)$ are the variances of the mixed noise and the SD noise, respectively. Since the mean value of the mixed noise is zero, the term $f(t,s,p)$ equals the mean value of $g(t,s,p)$. Moreover, because both SD and SI noise are stationary in each band, we can get the noise variance model for a particular band p as follows:

$$\sigma_{n,p}^2 = \sigma_{\text{si},p}^2 + \sigma_{\text{sd},p}^2 \cdot \mu(g(t,s,p)), \tag{7}$$

where $\mu(g(t,s,p))$ is the mean value of $g(t,s,p)$. $\sigma_{n,p}^2$, $\sigma_{\text{si},p}^2$, and $\sigma_{\text{sd},p}^2 \cdot \mu(g(t,s,p))$ denote the variances of the mixed noise, the SI noise, and the SD noise, respectively, in band p.

In particular, when $\sigma_{\text{sd},p}^2 = 0$, i.e., there is no SD noise in the image or the intensity of the SD noise is small enough to be ignored, this noise model is suitable for purely additive noise.

3. Noise Estimation Algorithm

The proposed algorithm exploits the strong correlation of signal data among spectral bands and inner homogeneous areas of the same band. The MLR model is utilized to remove the spectral and spatial correlations in homogeneous regions, where the mean square value of residuals are identified as the mixed noise variance in this band. The variances of SD and SI noise are calculated by a modified scatter plot approach. The crucial point of our algorithm is the accurate detection of homogeneous areas in the noisy image, which directly influences the accuracy of noise estimation. The proposed algorithm, hereafter called adaptive noise estimation (ANE), consists of three components, as shown in Fig. 1: A, detection of homogeneous areas; B, computation of mixed noise variances; and C, calculation of SD and SI noise variances.

A. Detection of Homogeneous Areas

HS images usually contain a large number of small homogeneous areas, where each area corresponds to a single object. Various region-growing-based algorithms have been proposed to detect homogeneous areas in images [24–26]. However, there are still
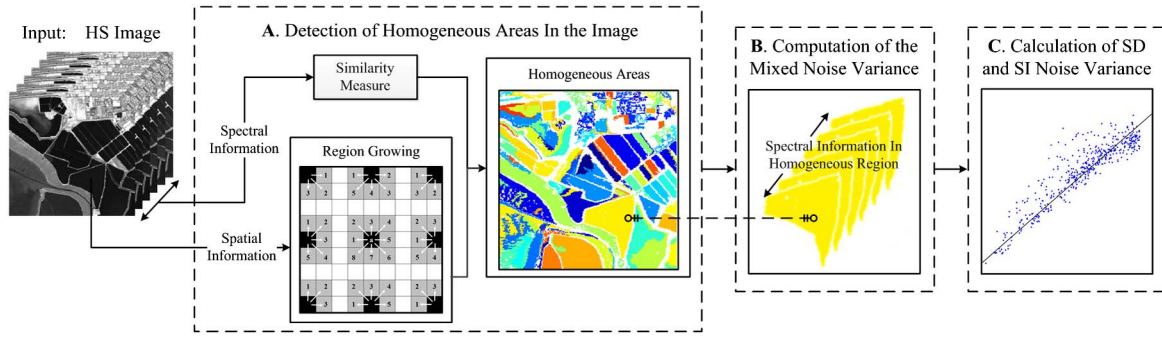
Fig. 1. Diagram of the proposed ANE.

two problems not properly addressed in the existing algorithms: one is the effectiveness and efficiency of homogeneous area detection in highly textured noisy images, and the other is the robustness of the similarity judgment of two pixels.

Euclidean distance (ED) and the spectral angle mapper (SAM) are two widely used similarity measures. Compared to ED, the advantage of SAM is that it is independent to spatial intensity fluctuations, so that the shape of the spectra, and not their amplitudes, are compared. Spectral information divergence (SID) is another similarity measure for HS images, and it is derived from the concept of divergence and has been demonstrated to be more efficient than SAM [27]. However, these similarity measures are still difficult to use to distinguish highly similar classes in noisy HS images. To solve the challenge, a hybrid metric [28] of SAM and SID is utilized in our algorithm.

The measure SAM calculates the angle between the spectra of two pixels, x and y as follows:

$$\mathrm{SA}(x,y) = \cos^{-1}\left(\frac{\sum_{p=1}^{P} x_p \cdot y_p}{\sqrt{\sum_{p=1}^{P} x_p^2} \cdot \sqrt{\sum_{p=1}^{P} y_p^2}}\right), \quad (8)$$

where P is the total band number of the HS data.

With regard to SID, the self-information of the spectra of pixels x and y should be first defined as

$$\begin{cases} I(x_p) = -\log h(x_p) \\ I(y_p) = -\log q(y_p) \end{cases}, \quad (9)$$

where $h(x_p) = x_p / \sum_{p=1}^{P} x_p$, and $q(y_p) = y_p / \sum_{p=1}^{P} y_p$. By using Eq. (9), the joint entropy $D(x(\|y)$ and $D(y(\|x)$ of x and y can be defined as

$$\begin{cases} D(x\|y) = \sum_{p=1}^{P} h(x_p) \log\left(\frac{h(x_p)}{q(y_p)}\right) \\ D(y\|x) = \sum_{p=1}^{P} q(y_p) \log\left(\frac{q(y_p)}{h(x_p)}\right) \end{cases}. \quad (10)$$

Finally, the SID of x and y can be calculated as

$$\mathrm{SID}(x,y) = D(x\|y) + D(y\|x)$$
$$= \sum_{p=1}^{P} (h(x_p) - q(y_p)) \log\left(\frac{h(x_p)}{q(y_p)}\right). \quad (11)$$

A mixed metric $z(x,y)$ combined with SAM and SID is utilized to degree the similarity of two pixels x and y in the proposed ANE, defined as

$$z(x,y) = \mathrm{SID}(x,y) \times \sin(\mathrm{SA}(x,y)). \quad (12)$$

Note that the SID models the spectrum of a HS image pixel as a probability distribution, so that spectral variations among spectral bands can be captured effectively in a stochastic manner. In contrast with the SID, the SA is a deterministic measure and considers a spectrum of a pixel vector as a vector rather than a probability distribution. The metric $z(x,y)$ takes advantage of the strengths of both SID and SAM in spectral dissimilarity, which has been proved to have a significant improvement over SAM and SID by experiments [28]. Moreover, the selection of threshold in the homogeneous-area-detection algorithm would benefit from this robust spectral metric.

Based on the similarity metric, we propose an automatic homogeneous-area-detection algorithm. First, a threshold ξ is predefined. The decision rule is that pixels x and y belong to the same area if $z(x,y) < \xi$. Otherwise, pixels x and y fall into two different regions. The new homogeneous-area-detection algorithm is presented in Algorithm 1.

Algorithm 1. Homogeneous Area Detection

Input: A HS image and a predefined threshold ξ
Output: Matrix S, indicating the class of each pixel
Initialization: $k = 0$, $Q = \{\varnothing\}$
  # Comments
while S contains unlabeled pixels **do**
    $k = k + 1$ # increase the class number
    $a_1 = a_0$ # a_0 is a randomly selected pixel from unlabeled pixels
    $Q = \{a_1\}$ # add a_1 into the queue Q
    while Q is not empty **do**
      $a_2 = Q.\mathrm{pop}$ # pop out a pixel from Q
      if $z(a_1, a_2) < \xi$
        $S(a_2) = k$ # label pixel a_2 as class k
        $A = Unlabeled(a_2)$ # select all unlabeled neighbors of a_2
        $Q = \{A\}$ # add all pixels in A into Q
      end
    end
  end
Return S

B. Computation of Mixed Noise Variances

When homogeneous areas in the HS image are detected, we make use of the MLR model to remove significant spatial and spectral correlations in each homogeneous region, considering the variance of residuals as the mixed noise variance. To estimate the mixed noise variance of band p in the HS data, pixels in adjacent bands $p-1$ and $p+1$ are utilized. Note that the first band and the last band of the HS data cannot be processed directly since they do not have two immediately adjacent bands. In practice, the first band and the last band are handled specially, where the pixel in the same location in only one adjacent band and a neighbor pixel in the same band are utilized for the MLR model. When dealing with the pixel $g(t,s,p)$ in a detected homogeneous area, the corresponding residual $r(t,s,p)$ is calculated as

$$r(t,s,p) = g(t,s,p) - \hat{g}(t,s,p), \tag{13}$$

in which $\hat{g}(t,s,p)$ is the value predicted for pixel $g(t,s,p)$ using the MLR model, which can be formulated as

$$\hat{g}(t,s,p) = ag(t,s,p-1) + bg(t,s,p+1) + cg(t',s',p) + d, \tag{14}$$

where a, b, c, and d are regression coefficients and $g(t',s',p)$ represents one of the neighbor pixels of $g(t,s,p)$ and belongs to the same homogeneous region. In our algorithm, the regression coefficients are estimated using the least-squares (LS) method, in which they are computed to minimize Λ^2, the sum of the squares of these residuals. Λ^2 is given by

$$\Lambda^2 = \sum_{t,s=1}^{M} r(t,s,p)^2, \tag{15}$$

where M is the number of pixels in the homogeneous area. $g(t',s',p)$ is obtained by sequentially scanning the eight neighbor pixels and determining whether each belongs to the same homogeneous region with $g(t,s,p)$. The computation time is reasonable as only one neighbor pixel in the same band is needed, so the first scanned pixel might be satisfied for most pixels that are exclusive of the boundaries of the homogeneous areas.

The mixed noise variance is calculated with an unbiased estimate of the variance of residuals in the homogeneous area:

$$\sigma_{n,p}^2 = \frac{1}{M-4}\Lambda^2. \tag{16}$$

Note that the degrees of freedom are reduced from M to $M-4$ as four parameters are utilized in the MLR model.
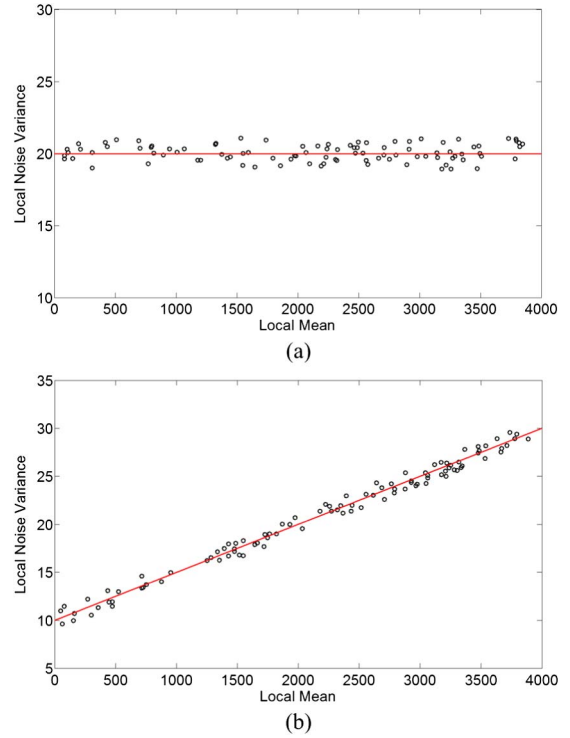

Fig. 2. Scatter plot diagrams of local means versus corresponding local noise variances and fitted by LSLF: (a) purely additive noise and (b) mixed noise.

C. Calculation of SD and SI Noise Variances

When the mixed noise variance of each homogeneous area is estimated with the MLR model, we aim to calculate variances of the SD and SI noise in band p by drawing a scatter plot of local mean versus corresponding local noise variance in homogeneous regions. According to Eq. (7), we can use slope and the y intercept to graph straight lines by using these points, which are equivalent to $\sigma_{\mathrm{si},p}^2$ and $\sigma_{\mathrm{sd},p}^2$, respectively. To fit the points in the scatter plot more accurately, the least squares linear fitting (LSLF) approach is utilized in our algorithm.

Moreover, noise type can be easily identified in terms of scatter plot: if the noise is purely additive, local noise variances are independent of local means in the homogeneous regions. Thus, the points in the scatter plot should be fitted as a horizontal line with slope equal to 0, where the intercept is the estimate of additive noise variance, as shown in Fig. 2(a). Provided that the noise is a mixture of the SD and SI noise components, the fitted line should be inclined, as shown in Fig. 2(b).

4. Experimental Results

In this section, performance of the ANE is evaluated by using both synthetic images and real AVIRIS images. The descriptions of the synthetic and real images are presented in Section A. In Section B, the quantitative evaluation metrics are illustrated to evaluate the algorithms with synthetic images.

In Section C, the ANE is applied to the synthetic images for comprehensive and quantitative experimental evaluations. In Section D, the ANE is applied to the real AVIRIS images with various complex land covers to evaluate the robustness of our algorithm. To further demonstrate the applicable performance of the ANE, we exploit our algorithm in the application of noise level estimation and noise type identification for AVIRIS images acquired in different periods in Section E.

A. Experimental Image Description

1. Synthetic Images

Five spectra are extracted from the real AVIRIS data to generate synthetic images, which are labeled as spectra x_1, x_2, x_3, x_4, and x_5. With the selected spectra, we have designed three synthetic HS image data sets as Data Set 1, Data Set 2, and Data Set 3, which are simulated with the first 90 bands of the selected spectra. Figures 3(a)–3(c) show typical examples of the 50th band for each data set. Data Sets 1 and 3 are generated with spectra x_1, x_2, x_3, and x_4 while Data Set 2 is simulated with all five spectra; each band has the uniform image size of 256×256. It can be clearly observed from Figs. 3(a)–3(c) that the three synthetic images have different complexities, deliberately designed for the evaluation of the

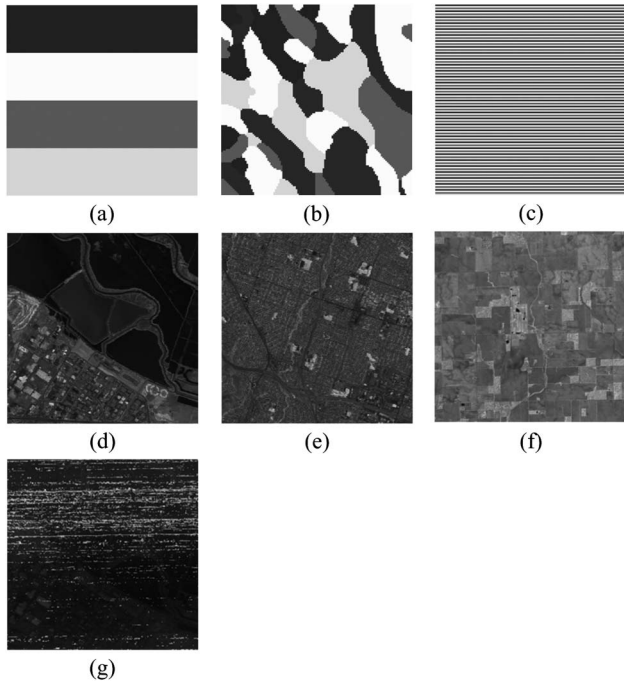(a) (b) (c)

(d) (e) (f)

(g)

Fig. 3. (a)–(c) Synthetic images and (d)–(f) AVIRIS images used in the experiments: (a) the 50th band of Data Set 1 with wide stripes, (b) the 50th band of Data Set 2 with camouflage pattern, (c) the 50th band of Data Set 3 with thick stripes, (d) the 60th band of Data Set 4 with simple structures acquired in the year 2008, (e) the 60th band of Data Set 5 with complex structures acquired in the year 2008, (f) the 60th band of Data Set 6 acquired in the year 1996, and (g) the 109th band of Data Set 4 mainly degraded by the pattern noise.

adaptability and robustness of the noise estimation algorithms.

2. AVIRIS Images

The AVIRIS measures sensor-reaching radiance in 224 spectral bands covering the spectral range from 400 to 2500 nm at 10 nm intervals. AVIRIS images have been widely used for research and applications since the late 1980s, when a detailed introduction of AVIRIS was reported in [3]. To assess the accuracy and adaptability of the ANE on real HS images with different complexities, two images with the size 256×256 are clipped from the same HS image acquired on 11/6/2008, and they are called Data Set 4 and Data Set 5. Thus, noise levels in Data Sets 4 and 5 are treated the same. Note that a part of image bands of AVIRIS data are not mainly degraded by random noise. For example, Fig. 3(g) shows the 109th band of Data Set 4, which is obviously mainly degraded by the pattern noise. To achieve better evaluation of the ANE, we select bands 11–94 and 131–224 from the 224 bands of Data Sets 4 and 5. The 60th bands of the two data sets are shown in Figs. 3(d) and 3(e), where Data Set 4 is highly textured in the lower half of the image but smoothed in the upper half, while Data Set 5 is all highly textured with abundant textures and edges.

One of the images utilized in the application of the ANE in Section E is Data Set 4 obtained in the year 2008; another one is an AVIRIS image acquired on 05/07/1996, where a small image is clipped from the entire HS data with the same image size and spectral bands as Data Set 4 for convenient comparison. We use the test image acquired in 1996 as Data Set 6 and its 60th band is shown in Fig. 3(f).

B. Quantitative Evaluation Metrics

Mixed noise is added to synthetic images according to the noise model. To set the values of noise parameters $\sigma_{si,p}^2$ and $\sigma_{sd,p}^2$ in each band, the signal-to-noise ratio (SNR) metric is utilized to measure the noise level. Moreover, a new measurement is defined to calculate the percentage of SD (PSD) noise component in the mixed noise. These two indicators are calculated as follows for the band p of a HS image:

$$\text{SNR}(p) = 20 \log_{10} \frac{\mu(g(t,s,p))}{\sigma_{n,p}}, \tag{17}$$

$$\text{PSD}(p) = \frac{\sigma_{sd,p}^2 \cdot \mu(g(t,s,p))}{\sigma_{n,p}^2}. \tag{18}$$

To quantitatively evaluate the performance of different algorithms, we define the relative-mean-square error (RMSE) of estimation results averaged over all 90 bands as $\bar{\varepsilon}_{sd}$, $\bar{\varepsilon}_{si}$, $\bar{\varepsilon}_{snr}$, and $\bar{\varepsilon}_{psd}$, which are calculated as follows

$$\bar{\varepsilon}_{\rm sd} = \frac{1}{P}\sum_{p=1}^{P}\varepsilon_{{\rm sd},p} = \frac{1}{P}\sum_{p=1}^{P}\left(\frac{\hat{\sigma}_{{\rm sd},p}^2 - \sigma_{{\rm sd},p}^2}{\sigma_{{\rm sd},p}^2}\right)^2, \quad (19)$$

$$\bar{\varepsilon}_{\rm si} = \frac{1}{P}\sum_{p=1}^{P}\varepsilon_{{\rm si},p} = \frac{1}{P}\sum_{p=1}^{P}\left(\frac{\hat{\sigma}_{{\rm si},p}^2 - \sigma_{{\rm si},p}^2}{\sigma_{{\rm si},p}^2}\right)^2, \quad (20)$$

$$\bar{\varepsilon}_{\rm snr} = \frac{1}{P}\sum_{p=1}^{P}\varepsilon_{{\rm snr}_p} = \frac{1}{P}\sum_{p=1}^{P}\left(\frac{\widehat{\rm SNR}_p - {\rm SNR}_p}{{\rm SNR}_p}\right)^2, \quad (21)$$

$$\bar{\varepsilon}_{\rm psd} = \frac{1}{P}\sum_{p=1}^{P}\varepsilon_{{\rm psd}_p} = \frac{1}{P}\sum_{p=1}^{P}\left(\frac{\widehat{\rm PSD}_p - {\rm PSD}_p}{{\rm PSD}_p}\right)^2, \quad (22)$$

where $\varepsilon_{\rm sd}$, $\varepsilon_{\rm si}$, $\varepsilon_{\rm snr}$, and $\varepsilon_{\rm psd}$ represent the estimation errors in band p. $\hat{\sigma}_{{\rm sd},p}^2$, $\hat{\sigma}_{{\rm si},p}^2$, $\widehat{\rm SNR}_p$, and $\widehat{\rm PSD}_p$ denote the estimation results, while $\sigma_{{\rm sd},p}^2$, $\sigma_{{\rm si},p}^2$, ${\rm SNR}_p$, and ${\rm PSD}_p$ are the corresponding true values.

C. Experiments on Synthetic Images

We have designed three experiments with synthetic images: (1) comparison of the accuracy and adaptability between the proposed ANE and another four existing algorithms when dealing with synthetic images with various complexities; (2) accuracy evaluation of the ANE when the synthetic images have different noise levels; and (3) accuracy evaluation of the ANE when the synthetic images have different percentages of SD noise component in the mixed noise.

1. Accuracy and Adaptability Evaluation with Compared Algorithms

In this experiment, mixed noise was added to each band of the three synthetic data sets with SNR = 30 dB and PSD = 0.5. The true values of $\sigma_{{\rm sd},p}^2$ and $\sigma_{{\rm si},p}^2$ in band p can be calculated according to Eqs. (17) and (18). Existing benchmarking and state-of-the-art algorithms were utilized for the comparison with the ANE, including the additive and multiplicative noise estimation algorithm (AMNE) [21], the HS noise parameter estimation algorithm (HYNPE) [17], the signal-dependent noise estimation algorithm (SDNE) [18], and the unsupervised signal-dependent noise estimation algorithm (USSDNE) [22].

First, the homogeneous-area-detection algorithm was applied to the noisy synthetic Data Sets 1–3, where the threshold was set as $\xi = 0.001$ based on the estimation performance. In our algorithm, only image areas with more than 50 pixels were utilized for noise estimation. The detected homogeneous regions are illustrated in Fig. 4, in which we use different colors for the corresponding regions. Figure 4 shows that the proposed homogeneous-area-detection algorithm performs well on images with
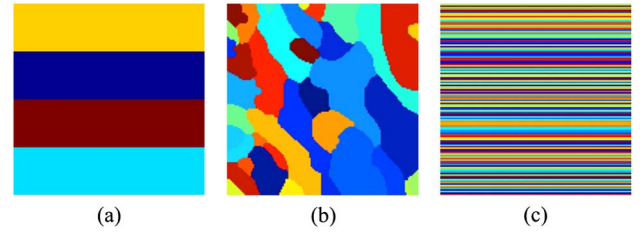

Fig. 4. Homogeneous-area-detection results in synthetic images with SNR = 30 dB and PSD = 0.5 by the ANE: (a) Data Set 1, (b) Data Set 2, and (c) Data Set 3.

various complexities, even when the image is seriously degraded by mixed noise.

The four compared algorithms were applied to the synthetic data in this experiment. Parameters in these algorithms were set according to the suggestions in their respective papers. However, a parameter L was required for image homogeneity identification in the USSDNE but has not been suggested. We set the parameter $L = 110$ when using the USSDNE based on the experimental results. Estimates of SD noise variance, SI noise variance, and SNR in each band with the four compared algorithms were evaluated with the true values. Figure 5 shows the experimental results with synthetic Data Set 2. Since no homogeneous identification step exists and no spectral information is utilized, the AMNE cannot
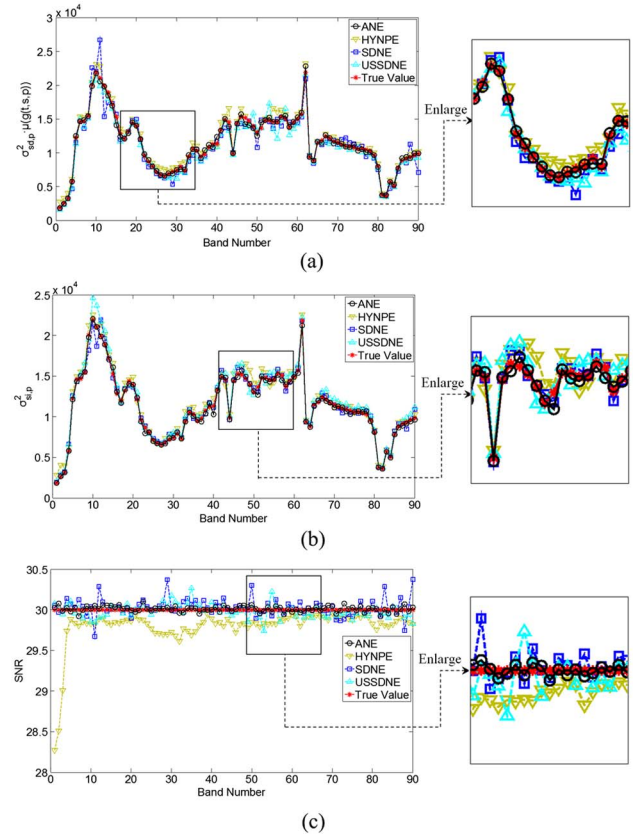

Fig. 5. Estimation results of each band in Data Set 2 using the ANE, AMNE, HYNPE, SDNE, and USSDNE algorithms: (a) SD noise variance; (b) SI noise variance; and (c) SNR.

Table 1. Values of ε_{sd}, ε_{si} and ε_{snr} with Data Sets 1–3 Using Different Algorithms[a]

		ANE	AMNE	HYNPE	SDNE	USSDNE
$\bar{\varepsilon}_{\text{sd}}$	Data Set 1	5.5×10^{-4}	6.0×10^{-4}	2.5×10^{-3}	3.1×10^{-3}	4.3×10^{-3}
	Data Set 2	7.8×10^{-4}	1.9×10^{3}	7.1×10^{-3}	7.0×10^{-3}	4.0×10^{-3}
	Data Set 3	7.9×10^{-4}	1.6×10^{7}	3.0×10^{-3}	—	2.9×10^{6}
$\bar{\varepsilon}_{\text{si}}$	Data Set 1	3.9×10^{-4}	4.2×10^{-4}	3.0×10^{-3}	1.3×10^{-3}	1.6×10^{-3}
	Data Set 2	5.9×10^{-4}	3.0×10^{3}	9.9×10^{-3}	1.7×10^{-3}	3.3×10^{-3}
	Data Set 3	4.6×10^{-4}	1.4×10^{7}	3.4×10^{-3}	—	1.3×10^{6}
$\bar{\varepsilon}_{\text{snr}}$	Data Set 1	6.1×10^{-7}	7.1×10^{-7}	2.7×10^{-5}	3.6×10^{-6}	1.2×10^{-5}
	Data Set 2	1.6×10^{-6}	2.8×10^{-1}	1.1×10^{-4}	1.4×10^{-5}	7.4×10^{-6}
	Data Set 3	1.3×10^{-6}	6.7×10^{-1}	2.7×10^{-5}	—	7.8×10^{-1}

[a]Results were obtained with SNR = 30 dB and PSD = 0.5.

effectively deal with highly textured images. In consideration of the figure scale and for a clear observation of the estimates with the other four algorithms, the results of the AMNE are removed from Fig. 5. The RMSEs of estimation results with all algorithms including the AMNE are calculated according to Eqs. (19)–(22) and recorded in Table 1, in which the best results are denoted in bold type.

Figure 5 shows that the proposed ANE produces more accurate results than the compared algorithms in most bands of Data Set 2. From the quantitative error results shown in Table 1, we shall further confirm that the ANE can estimate mixed noise accurately from images with various complexities and that it outperforms the other four algorithms. The algorithm AMNE performs well on Data Set 1 with simple structures. However, when the AMNE is applied to Data Set 2 and Data Set 3, the estimates increase excessively because too many image structures are regarded as noise. Thus, the AMNE is not suitable for highly textured images. The HYNPE can adaptively deal with both simple images and complex images as only spectral information is utilized in this algorithm. However, due to the absence of spatial information, the HYNPE produces less accurate estimates than our algorithm, even not as well as the SDNE and USSDNE. Unlike the AMNE and HYNPE, homogeneous image blocks are selected first in the SDNE and USSDNE. The utilization of spatial information in homogeneous regions makes it possible to estimate noise from highly textured images; however, the accuracy of the two algorithms depends mainly on the performances of their respective homogeneous block selection algorithms. Estimation results show that the SDNE and USSDNE perform similarly with Data Sets 1 and 2. When estimating noise from Data Set 2, they perform much better than the AMNE but are still not in competition with the proposed ANE. This is mainly because the homogeneous blocks are selected on each individual band in the SDNE and USSDNE. As a result, noise would be overestimated when textures and edges increase in images. The synthetic Data Set 3, designed as a pattern of horizontal strips two pixels wide, is actually too complex for the SDNE and USSDNE, in which it is difficult to find even one homogeneous block with the block size suggested in their papers. As a result, the SDNE was not applied to Data Set 3, and the estimation results of the USSDNE are incorrect.

2. Accuracy Evaluation with Various SNR

It has been demonstrated that the proposed ANE performs well on both simply textured and highly textured images with fixed noise intensity in the aforementioned experiment. However, the noise levels in real HS images always vary in a large range. Thus, we tested performance of the ANE when dealing with images with different noise levels.

We applied the proposed ANE to Data Set 2, which is degraded by mixed noise with PSD = 0.5. SNR is utilized as the indicator of noise level in each band with four different values: SNR = 25, 30, 35, and 40 dB. Estimation results and the true values of the SD noise variance, SI noise variance, and SNR in each band are plotted in Fig. 6. For a better quantitative analysis, we use $\bar{\varepsilon}_{\text{sd}}$, $\bar{\varepsilon}_{\text{si}}$, and $\bar{\varepsilon}_{\text{snr}}$ to evaluate the accuracy of the ANE, as listed in Table 2.

Figure 6 shows that the differences between the estimation results of the ANE and the true values are marginal for all bands when SNR = 30, 35, and 40 dB. Even when the value of SNR equals 25 dB, the estimation results are just a little biased from true values in a few bands. The quantitative errors in Table 2 demonstrate the aforementioned conclusion and indicate that when the value of SNR increases from 30 to 40 dB, the accuracy of our algorithm is very high and increases slightly.

3. Accuracy Evaluation with Various PSD

We simply assumed that the SD and SI noise contributed the same weight to mixed noise in the first two experiments. To evaluate the performance of the proposed ANE comprehensively, the value of SNR is fixed as 30 dB and different values of PSD are chosen to simulate the following five cases in this experiment:

(a) PSD = 0, the noise is purely additive;
(b) PSD = 0.25, the SI noise is dominant in the mixed noise;
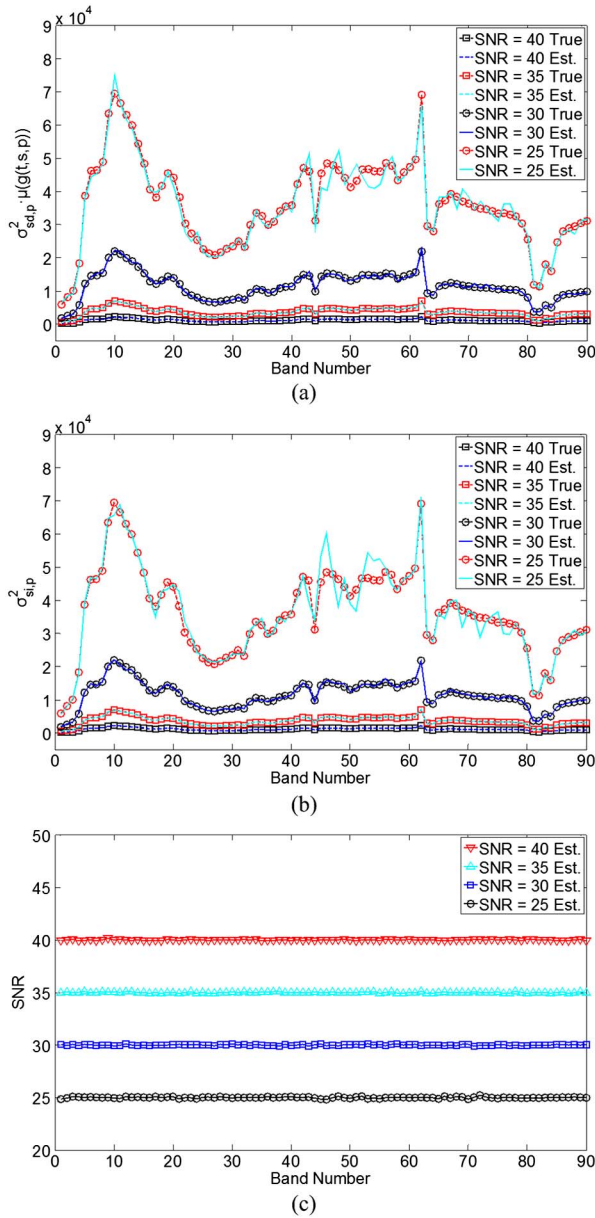(c) PSD = 0.5, the SD noise contributes the same as the SI noise;

Fig. 6. Estimation results of each band in Data Set 2 with different SNR: (a) SD noise variance; (b) SI noise variance; and (c) SNR.
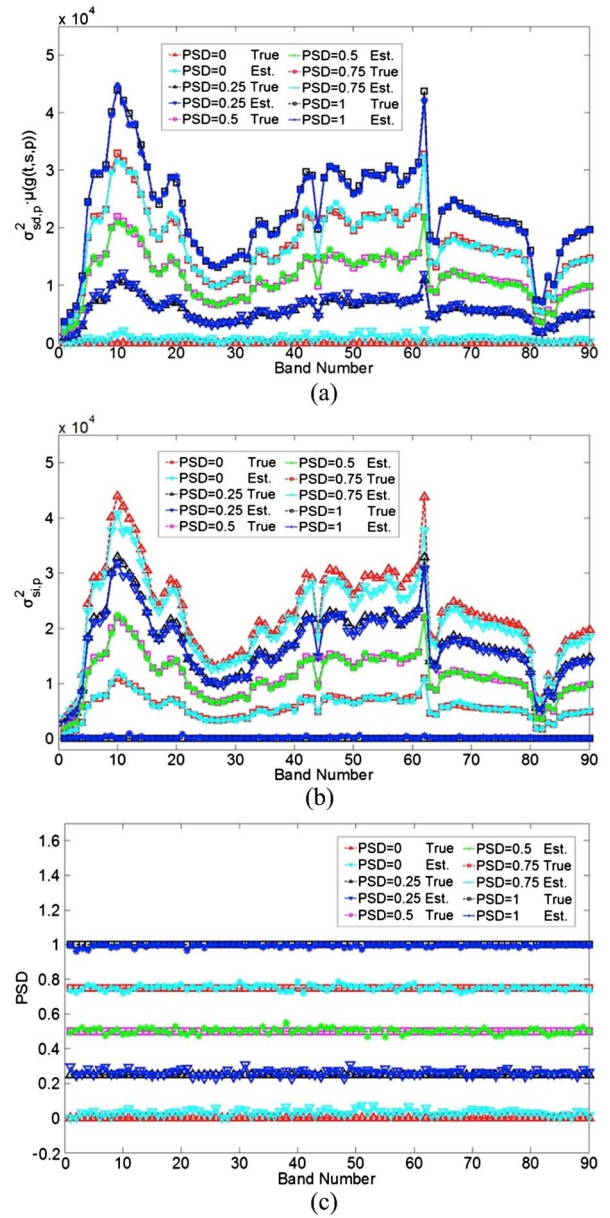

Fig. 7. Estimation results of each band in Data Set 2 with different PSD: (a) SD noise variance, (b) SI noise variance, and (c) PSD.

(d) PSD = 0.75, the SD noise is larger than the SI noise; and

(e) PSD = 1, the noise is purely signal dependent.

The estimation results of each band are plotted in Fig. 7 and the values of $\bar{\varepsilon}_{\mathrm{sd}}$, $\bar{\varepsilon}_{\mathrm{si}}$, and $\bar{\varepsilon}_{\mathrm{psd}}$ are recorded

Table 2. Values of ε_{sd}, ε_{si} and ε_{snr} with Data Set 2 Using the Proposed ANE[a]

SNR	25	30	35	40
$\bar{\varepsilon}_{\mathrm{sd}}$	3.3×10^{-3}	1.5×10^{-3}	1.3×10^{-3}	$\mathbf{1.3 \times 10^{-3}}$
$\bar{\varepsilon}_{\mathrm{si}}$	4.7×10^{-3}	9.3×10^{-4}	8.4×10^{-4}	$\mathbf{7.3 \times 10^{-4}}$
$\bar{\varepsilon}_{\mathrm{snr}}$	7.6×10^{-6}	3.1×10^{-6}	2.0×10^{-6}	$\mathbf{1.3 \times 10^{-6}}$

[a]Results were obtained with PSD = 0.5 and SNR = 25, 30, 35, and 40 dB.

in Table 3. Note that the measures $\bar{\varepsilon}_{\mathrm{sd}}$ and $\bar{\varepsilon}_{\mathrm{psd}}$ cannot be calculated when PSD = 0. Meanwhile, $\bar{\varepsilon}_{\mathrm{si}}$ is meaningless when PSD = 1. We can analyze using Fig. 7 and the rest of the quantitative measures in these special situations. For instance, the value of $\bar{\varepsilon}_{\mathrm{si}}$ helps to evaluate the performance of the ANE when PSD = 0. It is a better case when PSD = 1, as two indicators, $\bar{\varepsilon}_{\mathrm{sd}}$ and $\bar{\varepsilon}_{\mathrm{psd}}$, can be used.

It is observed from Fig. 7 and Table 3 that the proposed ANE performs well when percentage of the SD noise varies from 0 to 1. Quantitative errors in Table 3 indicate that the ANE produces the most accurate estimates of the SD noise variance and the PSD value when PSD = 1; when the SD noise equals the SI noise, the performance of the SI noise variance estimation is the best. The biggest deviation between

Table 3. Values of ε_{sd}, ε_{si} and ε_{psd} with Data Set 2 Using the Proposed ANE[a]

PSD	0	0.25	0.5	0.75	1
$\bar{\varepsilon}_{\mathrm{sd}}$	—	6.6×10^{-3}	1.3×10^{-3}	7.4×10^{-4}	$\mathbf{4.8 \times 10^{-4}}$
$\bar{\varepsilon}_{\mathrm{si}}$	3.9×10^{-3}	1.1×10^{-3}	$\mathbf{8.4 \times 10^{-4}}$	2.5×10^{-3}	—
$\bar{\varepsilon}_{\mathrm{psd}}$	—	6.9×10^{-3}	9.4×10^{-4}	3.4×10^{-4}	$\mathbf{1.1 \times 10^{-4}}$

[a]Results were obtained with SNR = 30 dB and PSD = 0, 0.25, 0.5, 0.75, and 1.

the estimate of the SI noise variance and the true value is found when the noise is purely signal independent. However, in this case, the value of $\bar{\varepsilon}_{\mathrm{si}}$ is 3.9×10^{-3}, which is accurate enough in practice [17]. Taken together, we shall conclude that the proposed ANE can adaptively estimate noise from images with different percentages of SD noise, even for the purely additive noise case.

D. Experiments on AVIRIS Images

1. *Identification of Noise Type*

First, we have checked the noise type and noise distribution in the AVIRIS data. Noise type is identified with the scatter plot of local noise variance versus local mean. Figure 8 shows the scatter plot of the 60th band in Data Set 4, from which we can claim that the noise type in the test data is mixed noise. We also plotted the noise distribution curve for the same band in Fig. 9, where the red curve is fitted with Gaussian distribution. The experimental results in Figs. 8 and 9 indicate that the noise model
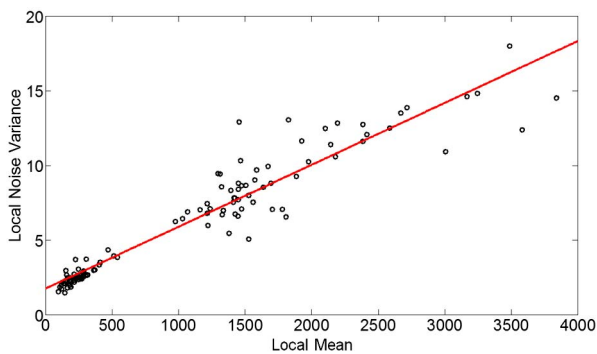

Fig. 8. Scatter plot of local means versus local noise variances in the 60th band of Data Set 4, where the red oblique line is fitted by using LSLF.
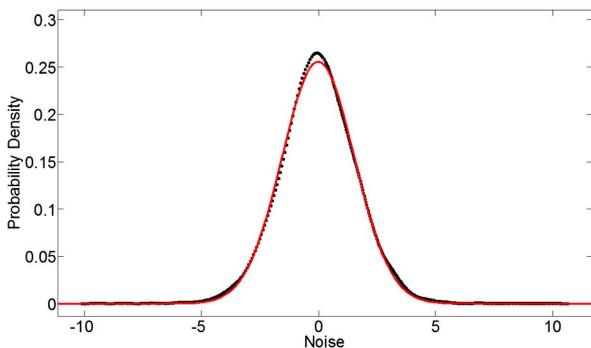

Fig. 9. Noise distribution in the 60th band of Data Set 4, where the red curve is fitted with Gaussian distribution.

exploited in our algorithm is suitable for the test AVIRIS data.

2. *Comparison between the ANE and USSDNE*

Based on the analysis of experimental results with the synthetic images, we found that the USSDNE is automatic and performs better than other three compared algorithms in the majority of the experimental datasets. As a result, the USSDNE is selected to compare with our algorithm in the experiments on real HS data. In the experiments of real images, we followed the same parameter settings in the synthetic images for USSDNE and ANE. In practise, the threshold ξ in our algorithm can be selected from 5×10^{-4} to 1.5×10^{-3} based on the estimation performance. For those highly textured images, we suggest to choose a smaller value since it is more capable of detecting homogeneous areas. Conversely, a larger value of ξ is recommended for simply textured images. Note that homogeneous area detection is very important for the two algorithms, where the results of homogeneous area detection with our algorithm are shown in Fig. 10, in which areas containing pixels less than 50 are drawn with white color. Meanwhile, homogeneous blocks selected using the USSDNE are exhibited in Fig. 11. We utilize the estimation results of the SI noise variance $\sigma_{\mathrm{si},p}^2$, SD noise variance $\sigma_{\mathrm{sd},p}^2 \cdot \mu(g(t,s,p))$ and mixed noise variance $\sigma_{n,p}^2$ to evaluate the performances of the compared algorithms. Estimates obtained by the ANE and USSDNE are presented in Fig. 12, from which we have the following three observations:

(1) When dealing with the simply textured Data Set 4, the estimation results with the ANE and USSDNE are similar. However, the estimates of SD noise variance obtained by the USSDNE are
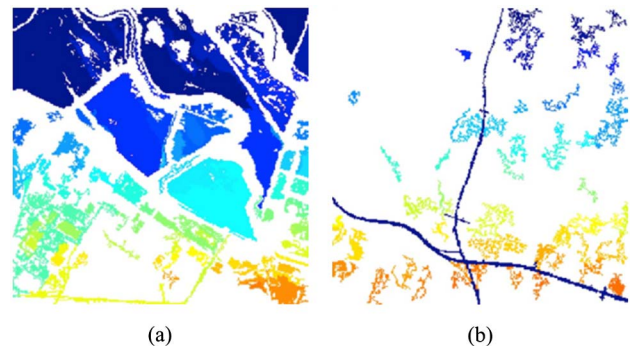

Fig. 10. Homogeneous-area-detection results with the ANE: (a) Data Set 4 and (b) Data Set 5.
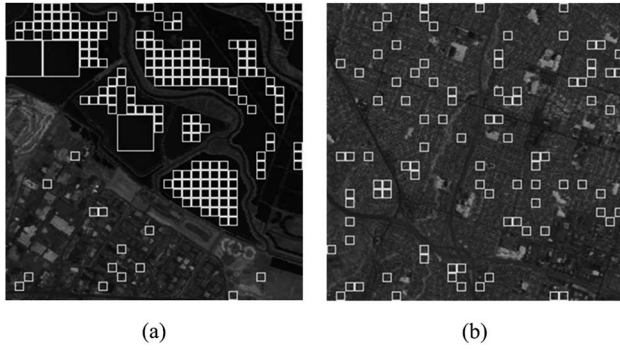
Fig. 11. Homogeneous-area-detection results with the USSDNE: (a) Data Set 4 and (b) Data Set 5.

slightly higher than that of the ANE in most bands. It can be explained with Fig. 11(a) that homogeneous blocks are well selected in the upper half of the image by using the USSDNE, but a few textured blocks are
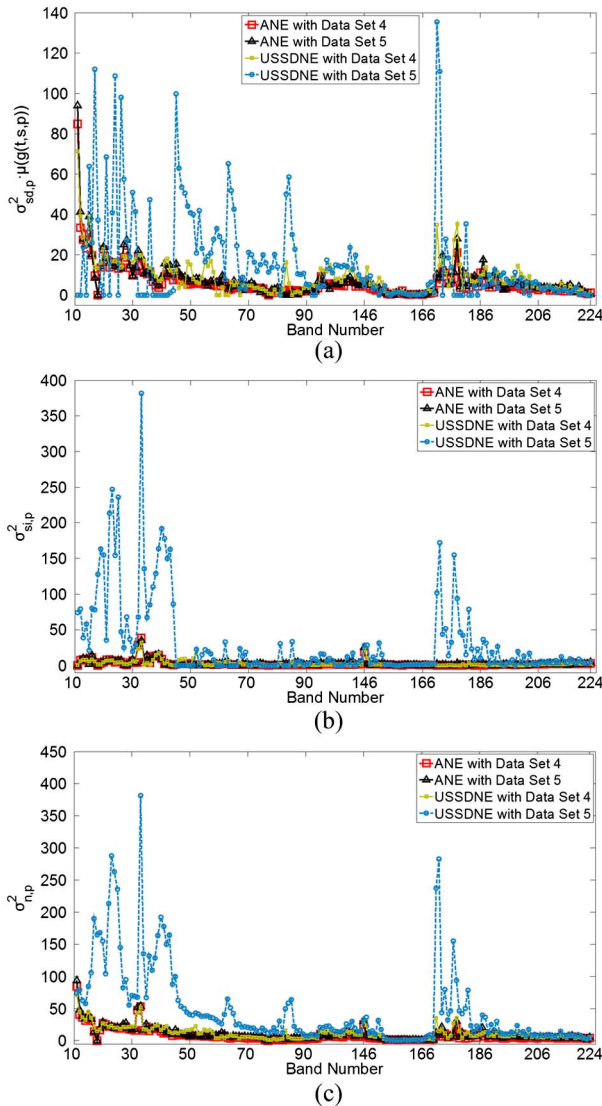

Fig. 12. Estimation results of each band in Data Sets 4 and 5 using the ANE and USSDNE. (a) SD noise variance, (b) SI noise variance, and (c) mixed noise variance.

mistaken for homogeneous ones in the lower half of the image, where image structures in these blocks bring about the over-estimation of the SD noise variance.

(2) The estimation results of Data Sets 4 and 5 are almost the same when using the proposed ANE. However, since it is extremely difficult to find rigid homogeneous areas in Data Set 5 with extremely complex image structures, the estimates of SD noise variances with Data Set 5 are a little larger than those with Data Set 4 in most bands. A marginal difference cannot deny the adaptability and robustness of the ANE when dealing with HS images with various complexities.

(3) The estimation results of Data Set 5 obtained by the USSDNE are abnormal in most bands. Obviously, accurate detection of homogeneous blocks in such highly textured images is very difficult for the USSDNE. Figure 11(b) shows that most of the selected homogeneous blocks are improper for an accurate noise estimation.

In summary, compared with the USSDNE, the proposed ANE is more adaptive and robust when dealing with real HS images with various complexities.

E. Application to AVIRIS Images Acquired in Different Periods

In this application, the proposed ANE was applied to two AVIRIS images acquired in different periods. The estimation results of noise type and noise level can be utilized to evaluate the image quality, and further reflect the running state of the imaging spectrometer in the corresponding periods. The estimates of the SI noise variance $\sigma_{\text{si},p}^2$, SD noise variance $\sigma_{\text{sd},p}^2 \cdot \mu(g(t,s,p))$, and mixed noise variance $\sigma_{n,p}^2$ are utilized to describe the noise in different data sets, which are exhibited in Fig. 13.

Experimental results in Fig. 13 indicate that both the SD noise variances and SI noise variances in Data Set 4 are smaller than those of Data Set 6 for most bands. As a result, the total mixed noise variances in Data Set 4 are smaller. The results illustrate that after 12 years improvement of the AVIRIS, the random noise in HS data has been significantly reduced. Hence, the imaging spectrometer provides higher quality images gradually, which is beneficial for the subsequent applications of the HS images.

Another significant task is to compare the percentages of SD components in the mixed noise for the two AVIRIS images acquired in 1996 and 2008. We define a new measure $\overline{\text{PSD}}$ by averaging the estimates of PSD over all the spectral bands for comparison. The values of $\overline{\text{PSD}}$ for Data Set 4 and 6 are equal to 0.69 and 0.39, respectively. This demonstrates that the noise in AVIRIS data acquired in 1996 and 2008 are both mixed noise. The difference is that, in the HS image acquired in 1996, the SI noise is dominant, while in the image acquired in 2008, the SD noise component contributes more weight. This can be explained by the generating mechanism of the SD noise
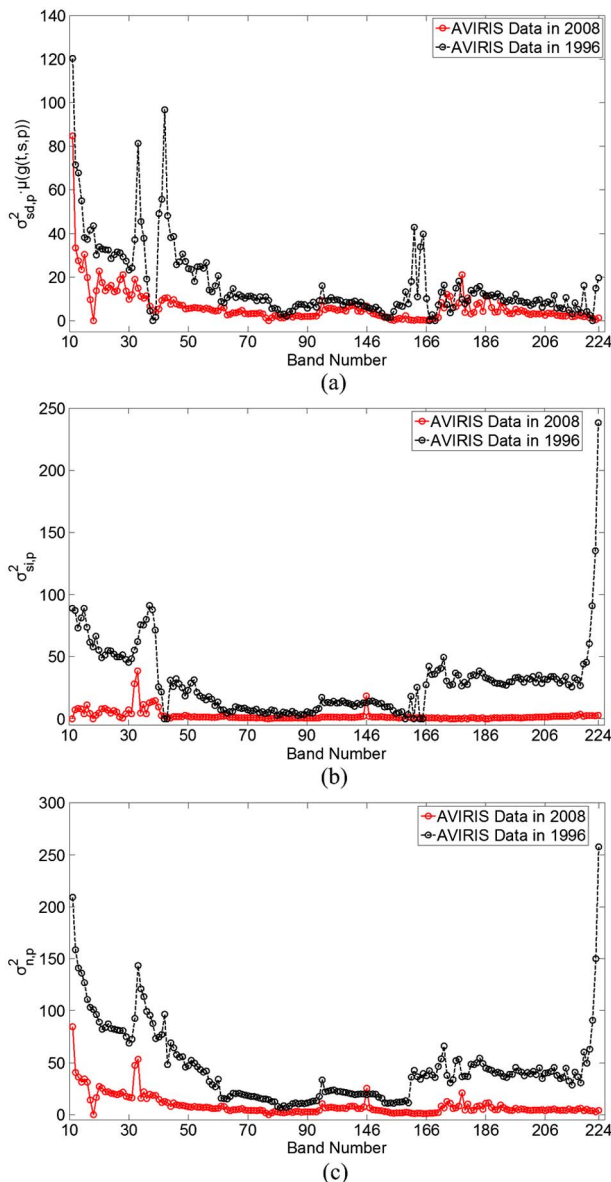
Fig. 13. Estimation results of each band in Data Sets 4 and 6 using the ANE: (a) SD noise variance; (b) SI noise variance; and (c) mixed noise variance.

as higher percentages of photonic noise are produced after the improvement of HS imaging spectrometer technology.

5. Conclusion

A fully automatic algorithm for noise estimation in HS images is proposed in this paper. The algorithm can adaptively estimate both mixed noise and purely additive noise from highly textured HS images. The proposed algorithm consists of three major steps: (1) homogeneous area detection in the HS image; (2) local mixed noise variance estimation based on MLR model; and (3) SD and SI noise split with a scatter plot approach.

It has been demonstrated that the performance of the proposed ANE are superior to the compared

benchmarking and state-of-the-art algorithms through experiments with synthetic images. Furthermore, the ANE is proved to be accurate and robust when the noise measures SNR and PSD vary in a wide range, even for the purely additive noise case. In the experiments with real AVIRIS data, the noise type and distribution in the AVIRIS images are shown to conform to the noise model in our algorithm. Experimental results indicate that the ANE is more adaptive and stable than the USSDNE when dealing with real HS images with various complexities.

Regarding computational cost, there are two aspects dominating the computational cost in our algorithm: the homogeneous-area-detection algorithm and mixed noise variance calculation using the MLR model. Compared with the SDNE and USSDNE, which process HS images from band to band, the ANE is much quicker because we select homogeneous areas with a spectral metric of all HS data. The HYNPE consumes less time because the HS data are also processed as a whole, which is similar to the ANE, but no spatial information is required in the HYNPE. However, the oversimplified process would make it less accurate than the proposed algorithm.

It is worth noting that, as the ANE exploits the strong correlation of image signal between spectral bands, the algorithm is ineffective for dealing with single band or multispectral images.

References

1. N. Acito, M. Diani, and G. Corsini, "On the CFAR property of the RX algorithm in the presence of signal-dependent noise in hyperspectral images," IEEE Trans. Geosci. Remote Sens. **51**, 3475–3491 (2013).
2. L. Gao, Q. Du, B. Zhang, W. Yang, and Y. Wu, "A comparative study on linear regression-based noise estimation for hyperspectral imagery," IEEE J. Sel. Top. Appl. Earth Observ. Remote Sens. **6**, 488–498 (2013).
3. R. O. Green, M. L. Eastwood, C. M. Sarture, T. G. Chrien, M. Aronsson, B. J. Chippendale, J. A. Faust, B. E. Pavri, C. J. Chovit, M. Solis, M. R. Olah, and O. Williams, "Imaging spectroscopy and the Airborne Visible/Infrared Imaging Spectrometer (AVIRIS)," Remote Sens. Environ. **65**, 227–248 (1998).
4. Y. Qian and M. Ye, "Hyperspectral imagery restoration using nonlocal spectral-spatial structured sparse representation with noise estimation," IEEE J. Sel. Top. Appl. Earth Observ. Remote Sens. **6**, 499–515 (2013).
5. D. Liu, X. Wang, J. Zhang, and X. Huang, "Feature extraction using Mel frequency cepstral coefficients for hyperspectral image classification," Appl. Opt. **49**, 2670–2675 (2010).

6. S. Bernabé, S. López, A. Plaza, and R. Sarmiento, "GPU implementation of an automatic target detection and classification algorithm for hyperspectral image analysis," IEEE Trans. Geosci. Remote Sens. **10**, 221–225 (2013).

7. B. Corner, R. Narayanan, and S. Reichenbach, "Noise estimation in remote sensing imagery using data masking," Int. J. Remote Sens. **24**, 689–702 (2003).

8. N. Fujimoto, Y. Takahashi, T. Moriyama, M. Shimada, H. Wakabayashi, Y. Nakatani, and S. Obayashi, "Evaluation of SPOT HRV image data received in Japan," in *Proceedings IEEE International Geoscience and Remote Sensing Symposium* (IEEE, 1989), pp. 463–466.

9. P. J. Curran and J. L. Dungan, "Estimation of signal-to-noise: a new procedure applied to AVIRIS data," IEEE Trans. Geosci. Remote Sens. **27**, 620–628 (1989).

10. B. Gao, "An operational method for estimating signal to noise ratios from data acquired with imaging spectrometers," Remote Sens. Environ. **43**, 23–33 (1993).

11. R. E. Roger and J. F. Arnold, "Reliably estimating the noise in AVIRIS hyperspectral images," Int. J. Remote Sens. **17**, 1951–1962 (1996).

12. L. Gao, B. Zhang, X. Zhang, W. Zhang, and Q. Tong, "A new operational method for estimating noise in hyperspectral images," IEEE Geosci. Remote Sens. Lett. **5**, 83–87 (2008).

13. P. Fu, Q. Sun, Z. Ji, and Q. Chen, "A new method for noise estimation in single-band remote sensing images," in *Proceedings IEEE International Conference on Fuzzy Systems and Knowledge Discovery* (IEEE, 2012), pp. 1664–1668.

14. J. Martin-Herrero, "Comments on 'A new operational method for estimating noise in hyperspectral images'," IEEE Geosci. Remote Sens. Lett. **5**, 705–709 (2008).

15. P. Fu, C. Li, Q. Sun, W. Cai, and D. Feng, "Image noise level estimation based on a new adaptive superpixel classification," to be presented at the 2014 IEEE International Conference on Image Processing.

16. J. Meola, M. T. Eismann, R. L. Moses, and J. N. Ash, "Modeling and estimation of signal-dependent noise in hyperspectral imagery," Appl. Opt. **50**, 3829–3846 (2011).

17. N. Acito, M. Diani, and G. Corsini, "Signal-dependent noise modelling and model parameter estimation in hyperspectral images," IEEE Trans. Geosci. Remote Sens. **49**, 2957–2971 (2011).

18. L. Alparone, M. Selva, B. Aiazzi, S. Baronti, F. Bufera, and L. Chiarantini, "Signal-dependent noise modelling and estimation in new-generation imaging spectrometers," in *Proceedings IEEE 1st Workshop on Hyperspectral Image and Signal Processing: Evolution in Remote Sensing* (IEEE, 2009), pp. 1–4.

19. M. Uss, B. Vozel, V. Lukin, and K. Chehdi, "Local signal-dependent noise variance estimation from hyperspectral textural images," IEEE J. Sel. Top. Signal Process. **5**, 469–486 (2011).

20. A. Foi, M. Trimeche, V. Katkovnik, and K. Egiazarian, "Practical Poissonian-Gaussian noise modelling and fitting for single image raw-data," IEEE Trans. Image Process. **17**, 1737–1754 (2008).

21. J. S. Lee and K. Hoppel, "Noise modeling and estimation of remotely sensed images," in *Proceedings IEEE International Geoscience and Remote Sensing Symposium* (IEEE, 1998), pp. 1005–1008.

22. B. Aiazzi, L. Alparone, S. Baronti, M. Selva, and L. Stefani, "Unsupervised estimation of signal-dependent CCD camera noise," EURASIP J. Adv. Signal Process. **2009**, 231 (2009).

23. P. Koczyk, P. Wiewior, and C. Radzewicz, "Photon counting statistics-undergraduate experiment," Am. J. Phys. **64**, 240–245 (1996).

24. S. Zhu and A. Yuille, "Region competition: unifying snakes, region growing, and Bayes/MDL for multiband image segementation," IEEE Trans. Pattern Anal. Mach. Intell. **18**, 884–900 (1996).

25. Q. Yu and D. A. Clausi, "IRGS: image segmentation using edge penalties and region growing," IEEE Trans. Pattern Anal. Mach. Intell. **30**, 2126–2139 (2008).

26. A. K. Qin and D. A. Clausi, "Multivariate image segmentation using semantic region growing with adaptive edge penalty," IEEE Trans. Image Process. **19**, 2157–2170 (2010).

27. C. I. Chang, "Spectral information divergence for hyperspectral image analysis," in *Proceedings of IEEE International Geoscience and Remote Sensing Symposium* (IEEE, 1999), pp. 509–511.

28. Y. Du, C. Chang, H. Ren, C. Chang, J. O. Jensen, and F. M. D'Amico, "New hyperspectral discrimination measure for spectral characterization," Opt. Eng. **43**, 1777–1786 (2004).